One-dimensional finite element grids based on a localized truncation error analysis

S. C. Hagen[a],*, J. J. Westerink[b] and R. L. Kolar[c]

[a] *Department of Civil and Environmental Engineering, University of Central Florida, Orlando, FL 32816-2450, USA*
[b] *Department of Civil Engineering and Geological Sciences, University of Notre Dame, Notre Dame, IN 46556, USA*
[c] *School of Civil Engineering and Environmental Science, University of Oklahoma, Norman, OK 73019-0631, USA*

SUMMARY

With the exponential increase in computing power, modelers of coastal and oceanic regions are capable of simulating larger domains with increased resolution. Typically, these models use graded meshes wherein the size of the elements can vary by orders of magnitude. However, with notably few exceptions, the graded meshes are generated using criteria that neither optimize placement of the node points nor properly incorporate the physics, as represented by discrete equations, underlying tidal flow and circulation to the mesh generation process. Consequently, the user of the model must heuristically adjust such meshes based on knowledge of local flow and topographical features—a rough and time consuming proposition at best. Herein, a localized truncation error analysis (LTEA) is proposed as a means to efficiently generate meshes that incorporate estimates of flow variables and their derivatives. In a one-dimensional (1D) setting, three different LTEA-based finite element grid generation methodologies are examined and compared with two common algorithms: the wavelength to Δx ratio criterion and the topographical length scale criterion. Errors are compared on a per node basis. It is shown that solutions based on LTEA meshes are, in general, more accurate (both locally *and* globally) and more efficient. In addition, the study shows that the first four terms of the ordered truncation error series are in direct competition and, subsequently, that the leading order term of the truncation error series is not necessarily the dominant term. Analyses and results from this 1D study lay the groundwork for developing an efficient mesh generating algorithm suitable for two-dimensional (2D) models. Copyright © 2000 John Wiley & Sons, Ltd.

KEY WORDS: finite elements; shallow water equations; truncation error analysis; grid generation

1. INTRODUCTION

Recent advances have permitted the development and the successful implementation of coastal ocean circulation models for increasingly larger domains [1–14]. While a large domain, such as the Western North Atlantic Tidal (WNAT) model domain shown in Figure 1, increases the

---

* Correspondence to: Department of Civil and Environmental Engineering, University of Central Florida, College of Engineering, P.O. Box 162450, Orlando, FL 32816-2450, USA.

predictive capabilities of coastal ocean models [9,10], it complicates the process of computa-tional node placement. However, the actual gridding of larger, more complex domains has not received the attention it deserves. This issue is addressed herein with the presentation of a grid generation method that more successfully couples the physics, as represented by discrete equations, underlying tidal flow and circulation to the mesh generation process.

Larger domains warrant a method of gridding that utilizes unstructured meshes, e.g. the finite element method, which allows for spatially-varying levels of discretization. Because, in
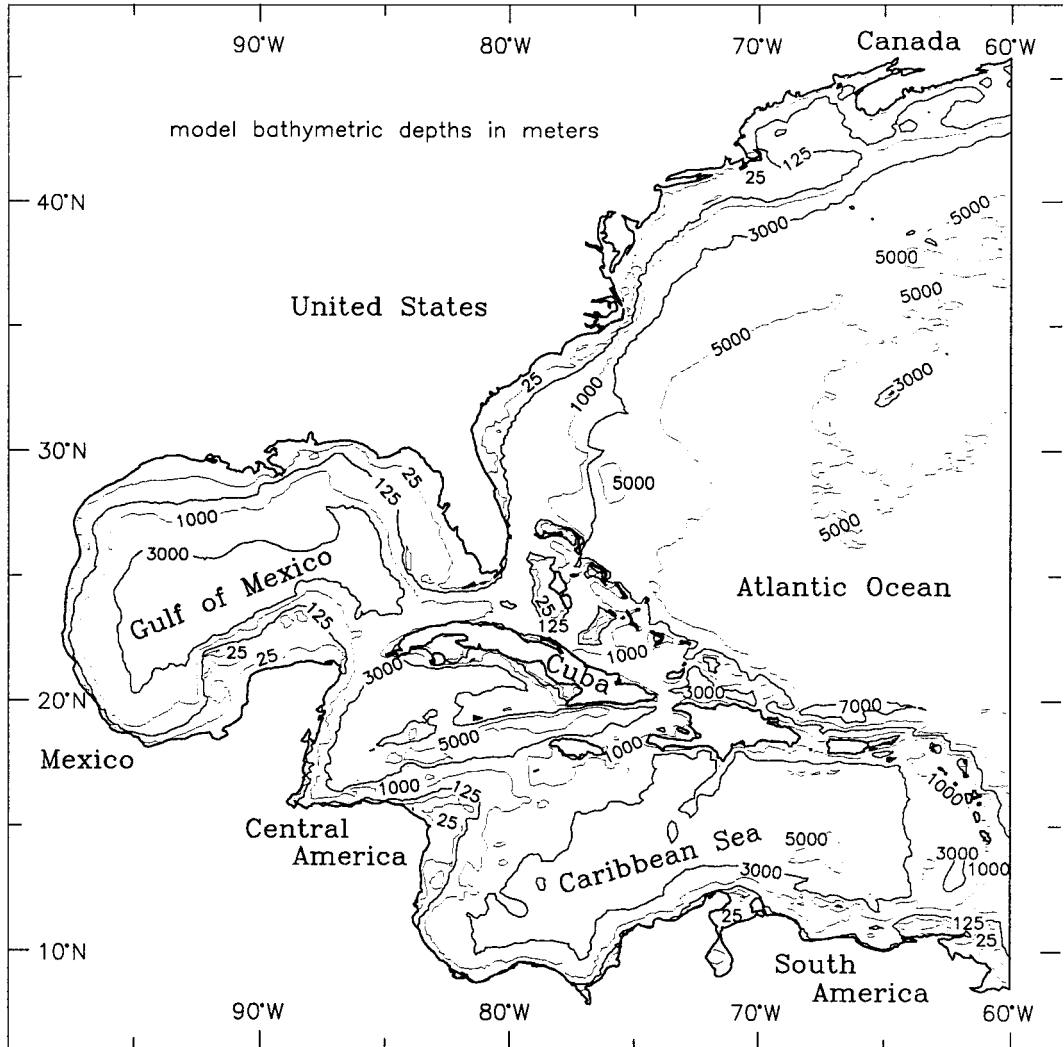

Figure 1. The WNAT model domain including bathymetry (in m).

general, shallower water has a higher localized wave number content than deeper water, higher resolution is required in shallow water regions. Furthermore, it has been shown that the computed response is highly sensitive to grid resolution in regions with steep bathymetric gradients [11,13,14]. Two-dimensional (2D) response structures associated with intricate shore-lines, 2D topography, amphidromes and resonant bays also require local refinement of grids. Conversely, deep ocean waters usually result in large expanses with more slowly-varying response structures in space, which can utilize a coarser level of resolution. These consider-ations indicate that variably-graded meshes are needed; these are easily implemented with the finite element method.

Currently, the method of production of variably-graded meshes for coastal ocean circulation models is poorly defined, imprecise and *ad hoc*. It is a tedious process at best. Because no robust criterion or node spacing routine exists that incorporates all of the aforementioned physical characteristics and subsequent responses into the mesh generation process, modelers are left to rely on their knowledge of particular domains and their intuition. For a large and complicated domain (Figure 1), this is a daunting task.

A widely used strategy to initiate variably-graded grids utilizes the wavelength to grid size ratio criterion for one-dimensional (1D), linear, frictionless, constant topography flow. This ratio is computed as:

$$\frac{\lambda}{\Delta x} = \frac{\sqrt{gh}}{\Delta x} T, \tag{1}$$

where g = gravitational constant, h = water depth and T = tidal period of interest. The ratio is set to some constant value—usually 40 or less—and an initial grid is generated [10,15]. The mesh is then manually edited to suit the modeler's needs. Local areas with a high rate of bathymetric change, such as the shelf break, the relatively steep continental slope and the continental rise, are not properly resolved by the wavelength to grid size ratio criterion [10–14]. Furthermore, this criterion does not recognize the 2D structure of the tidal response associated with intricate shorelines, continental shelf waves, Kelvin waves and amphidromes.

Hanna and Wright [16] recently proposed a new 1D criteria. The topographic length scale relation computes grid size such that

$$\Delta x \leq \frac{\alpha h}{h_{,x}}, \tag{2}$$

where h = water depth, $h_{,x}$ = the bathymetric slope and α, the mesh generation criterion, is set to some constant value such that $\Delta h/h \leq \alpha$ over any element. The topographic length scale relation incorporates bathymetry and the gradient of bathymetry into the mesh generation process. However, this criterion fails in the limit as $h_{,x} \to 0$. Thus, when no gradient in bathymetry exists, e.g. locally constant depth regions, $\Delta x = \infty$, which is clearly unreasonable. In addition, the TLS criterion does not take into account changes in the sea surface elevation or velocity field.

Grid generation techniques for the Navier–Stokes equations often involve the use of adaptive mesh refinement. Typically, these techniques require the calculation of some error

norm over an element. The error norm, in conjunction with the refinement algorithm, defines whether the element should be refined, stay the same, or be combined with neighboring elements to coarsen the resolution. Many different *a posteriori* error estimators are used for Navier–Stokes flow [17–21]. These local grid refinement algorithms typically examine the error in the computed response. They are not particularly well-suited for long wave propagation problems because the identification of localized error in the solution and subsequent local refinement does not necessarily improve the global solution. In fact, as will be shown in this paper, for the shallow water equations, the error source does not necessarily correspond with the region where errors in the response are most significantly manifested.

Alternatively, the localized truncation error analysis (LTEA) proposed in this paper examines the error produced by discretizing the governing equations, instead of focussing on the solution error. The LTEA procedure is still an *a posteriori* error estimation procedure because it includes approximations to the variables being simulated and their derivatives. Thus, an LTEA-based node placement routine directly couples estimated errors with the actual mesh generation process.

Four major topics are outlined in the paper. First, the 1D model, domain and a convergence study are presented. The second major topic includes the development of the local truncation error series representation, the examination of the first- through the fourth-orders of the truncation error series, and a description of the subsequent node spacing generation routine. Third, three methods for LTEA-based grid generation are presented: (1) a strict interpretation of localized node spacing requirements; (2) use of an imposed maximum multiple of change (a limit on the percentage one element can vary from its neighbor); and (3) a more practical method that will permit extension of this routine to 2D problems. The final topic is the conclusions.

2. MODEL FORMULATION

The governing equations are the generalized wave continuity equation (GWCE) and the non-conservative momentum equation [3,5]. The linearized 1D GWCE is given by

$$\frac{\partial^2 \eta}{\partial t^2} + \tau_0 \frac{\partial \eta}{\partial t} - g \frac{\partial}{\partial x}\left(h \frac{\partial \eta}{\partial x}\right) - (\tau - \tau_0)\frac{\partial}{\partial x}(uh) = 0 \tag{3}$$

and the linearized, non-conservative momentum equation is expressed as

$$\frac{\partial u}{\partial t} + g \frac{\partial \eta}{\partial x} + \tau u = 0, \tag{4}$$

where t = time, x = space coordinate, η = the deviation of the free surface from the geoid, u = velocity in the x-direction, τ_0 = a weighting parameter in the GWCE, which controls the primitive continuity contribution, g = gravitational acceleration, h = depth relative to the geoid and τ = bottom friction coefficient.

All simulations performed herein utilize a finite element discretization of Equations (3) and (4) in space with linear Galerkin finite elements and a finite difference discretization in time [5]. Equation (3) is temporally discretized using a variably weighted, three-time-level, implicit scheme while Equation (4) is discretized in time using a two-time-level implicit Crank–Nicholson approximation [5]. In addition, all simulations performed herein utilize standard boundary conditions: a periodic elevation forcing with an amplitude of 1 m and a period of 12.42 h is implemented on the open ocean boundary and a no-flow boundary condition is enforced on the land boundary. Results are analyzed for the amplitude and the phase at each computational grid node.

3. 1D DOMAIN AND A COMPARISON SOLUTION

This study of 1D LTEA-based finite element grids requires a standard domain and an associated comparison solution. Because the WNAT model domain (Figure 1) is the focus of current research efforts [9–12], bathymetry that is typical of a slice taken perpendicular to the east coast of the US, extending out into the deep ocean (Figure 2), is chosen. The depth at the coast ($x = 0$ in Figure 2) is 20 m. The bathymetry declines linearly to a depth of 200 m, at a distance of 221 km from the coast (Figure 2, continental shelf break). The depth increases, but now at a steeper linear slope, until it reaches a depth of 4000 m at a distance of 329.8 km from the shore (toe of the continental slope). A more gradual linear slope follows until the deep ocean depth of 5000 m (assumed constant) is attained at a distance of 483.8 km from the shore (toe of the continental rise).

An approximate solution is used herein to estimate the derivatives for local truncation errors and to provide a basis to compare solutions from other meshes. Hereafter, this will be called the 'comparison solution'. Table I provides spatial and temporal detail for the regular grids
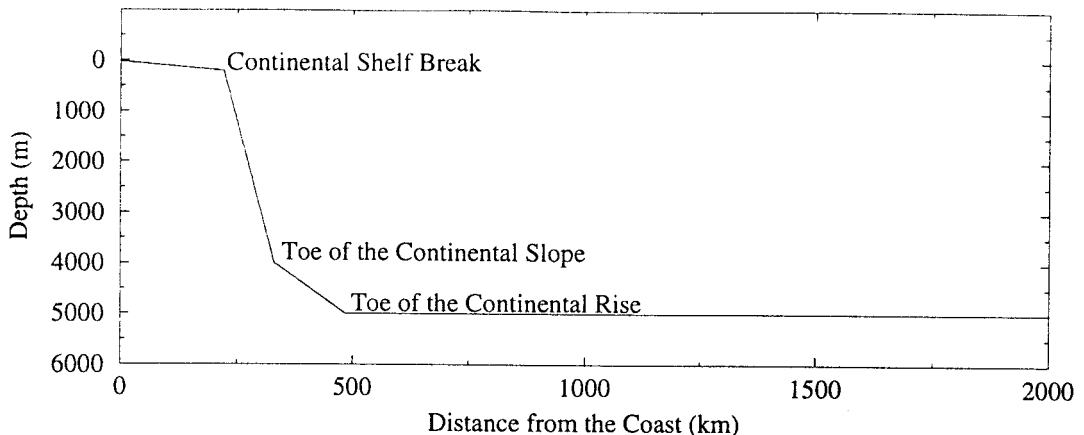

Figure 2. 1D idealized bathymetry.

Table I. Grids used for the comparison study

Grid	Spacing (km)	Number of nodes	Time step (s)
R.25	0.25	8001	1
R1	1.00	2001	4

(constant spacing) that are used with the domain of Figure 2 to verify and establish a comparison solution. Simulations of 10 days of real time are performed and harmonic solutions are obtained for each of the two meshes. Amplitude errors are normalized as

$$\varepsilon_A(x) = \frac{A_c(x) - A_f(x)}{A_f(x)}, \tag{5a}$$

with $A_c(x) =$ coarse grid amplitude solution (the R1 grid in this case) and $A_f(x) =$ fine grid amplitude solution (the R.25 grid in this case). Phase errors are computed in an absolute sense as

$$\varepsilon_\theta(x) = \theta_c(x) - \theta_f(x), \tag{5b}$$

with $\theta_c(x) =$ coarse grid phase solution (the R1 grid in this case) and $\theta_f(x) =$ fine grid phase solution (the R.25 grid in this case).

Equations (5a) and (5b) are then individually applied to a generalized Richardson extrapolation based error estimate [22]

$$E_{R.25}(x) = F_s \frac{|\varepsilon(x)|}{r^p - 1}, \tag{6}$$

where $F_s =$ a factor of safety, $r =$ grid refinement ratio and $p =$ the leading order of accuracy for the method used. Because two regularly spaced grids are evaluated, both of which would exhibit second-order-accuracy, $p = 2$ is applied, with $F_s = 1.25$ (as recommended by P.J. Roache, personal communication, 1996).

Equation (6) is computed at each node of grid R.25 and results in the error estimates shown in Table II, the maximum value of Equation (6) over the entire domain (Table II, Peak) and the average value of Equation (6) (Table II, Average). This table shows that the comparison

Table II. Richardson extrapolation based errors associated with Grid R.25

Error	Peak	Average
Velocity amplitude	$2.44 \times 10^{-1}\%$	$6.34 \times 10^{-4}\%$
Velocity phase	6.58×10^{-6} rad.	5.33×10^{-7} rad.
Elevation amplitude	$1.76 \times 10^{-4}\%$	$3.48 \times 10^{-5}\%$
Elevation phase	6.54×10^{-6} rad.	4.46×10^{-7} rad.

solution from the R.25 grid is a valid basis for use as a benchmark in this 1D study, because a converging solution of sufficient accuracy is indicated. Solutions from the R.25 grid are used in all subsequent absolute and relative error analyses. R1 grid velocity and elevation amplitude and phase solutions are used to approximate derivatives in the following truncation error series analyses.

4. TRUNCATION ERROR DEVELOPMENT

A harmonic form of the linearized, non-conservative momentum equation is obtained by substituting into Equation (4) $u = \hat{u} e^{\hat{i}\omega t}$ and $\eta = \hat{\eta} e^{\hat{i}\omega t}$, where $\hat{u}, \hat{\eta} =$ the complex amplitudes of u and η, $\hat{i} = \sqrt{-1}$ and $\omega =$ the response frequency. The linearized, non-conservative momentum equation is expressed in harmonic form as

$$\hat{i}\omega\hat{u} + g \frac{\partial\hat{\eta}}{\partial x} + \tau\hat{u} = 0. \tag{7}$$

Equation (7) is spatially discretized by using linear Galerkin finite elements. For a typical interior node, the linear, harmonic momentum equation becomes

$$\frac{\hat{i}\omega + \tau}{6} (\Delta_i\hat{u}_{j-1} + 2\Delta_i\hat{u}_j + 2\Delta_{i+1}\hat{u}_j + \Delta_{i+1}\hat{u}_{j+1}) + \frac{g}{2} (-\hat{\eta}_{j-1} + \hat{\eta}_{j+1}) = 0, \tag{8}$$

where $\Delta_i = x_j - x_{j-1}$ with $x_j = x$-coordinate at node j, $\hat{\eta}_j \equiv \hat{\eta}(x)|_{x=x_j}$ and $\hat{u}_j \equiv \hat{u}(x)|_{x=x_j}$, with $i = j - 1$ and $j = 2, N-1$ ($N =$ the total number of nodes).

The truncation error series is developed by: (1) substituting in Taylor Series expansions for all nodal variables of Equation (8); (2) separating the spatial orders; and (3) subtracting the continuous form of the linear, harmonic momentum Equation (7). What follows is the truncation error series representation, up to the fourth-order, for the linearized, harmonic form of the non-conservative momentum equation, for variable grids (where elemental length Δ_i may or may not be equal to adjacent elemental length Δ_{i+1}):

$$\tau_{ME} = \left(\frac{\hat{i}\omega + \tau}{6}\right) \left[2(\Delta_{i+1} - \Delta_i) \frac{\partial\hat{u}_j}{\partial x} + \left(\frac{\Delta_i^3 + \Delta_{i+1}^3}{\Delta_i + \Delta_{i+1}}\right) \frac{\partial^2\hat{u}_j}{\partial x^2} + \frac{1}{3} (\Delta_{i+1} - \Delta_i)(\Delta_i^2 + \Delta_{i+1}^2) \frac{\partial^3\hat{u}_j}{\partial x^3} \right.$$

$$+ \frac{1}{12} \left(\frac{\Delta_i^5 + \Delta_{i+1}^5}{\Delta_i + \Delta_{i+1}}\right) \frac{\partial^4\hat{u}_j}{\partial x^4} \left] + \frac{g}{6} \right[3(\Delta_{i+1} - \Delta_i) \frac{\partial^2\hat{\eta}_j}{\partial x^2} + \left(\frac{\Delta_i^3 + \Delta_{i+1}^3}{\Delta_i + \Delta_{i+1}}\right) \frac{\partial^3\hat{\eta}_j}{\partial x^3}$$

$$+ \frac{1}{4} (\Delta_{i+1} - \Delta_i)(\Delta_i^2 + \Delta_{i+1}^2) \frac{\partial^4\hat{\eta}_j}{\partial x^4} + \frac{1}{20} \left(\frac{\Delta_i^5 + \Delta_{i+1}^5}{\Delta_i + \Delta_{i+1}}\right) \frac{\partial^5\hat{\eta}_j}{\partial x^5} \right] + \text{H.O.T.} \tag{9}$$

For regular grids ($\Delta_i = \Delta_{i+1} = \Delta$):

$$\tau_{ME} = \frac{\hat{i}\omega + \tau}{6} \left(\Delta^2 \frac{\partial^2\hat{u}_j}{\partial x^2} + \frac{\Delta^4}{12} \frac{\partial^4\hat{u}_j}{\partial x^4} \right) + \frac{g}{6} \left(\Delta^2 \frac{\partial^3\hat{\eta}_j}{\partial x^3} + \frac{\Delta^4}{20} \frac{\partial^5\hat{\eta}_j}{\partial x^5} \right) + \text{H.O.T.}, \tag{10}$$

where $\hat{u}_j \equiv \hat{u}(x)|_{x=x_j}$ and $\hat{\eta}_j \equiv \hat{\eta}(x)|_{x=x_j}$. With Equations (9) or (10), the truncation error at any node j may be computed, provided the node spacings to the left (Δ_i) and the right (Δ_{i+1}) of node j are known. Examination of Equations (9) and (10) reveals that as Δ_i approaches Δ_{i+1}, the odd-order truncation terms become less significant and ultimately cancel out when Δ_i is equal to Δ_{i+1}.

All local truncation errors and local node spacing requirements presented herein are estimated using the truncation error for the non-conservative momentum Equation (9). Three major reasons form the basis for this decision: (1) the GWCE incorporates the momentum equation; (2) a separate study, not included in this paper in the interests of simplicity and brevity, indicates that the gradients of $\hat{\eta}$ are more important than the gradients of h in the truncation error series [14]; and (3) gradients of $\hat{u}$ dominate in shallow water, especially on the shelf and near the shore.

Partial derivatives of $\hat{u}_j$ and $\hat{\eta}_j$ from Equation (9) are approximated with central differences by applying the harmonic solutions from the R1 grid simulation at the nodes of the R1 grid [14]. Equation (9), the local truncation error, is estimated by incorporating the Δ_i values associated with a variable or a regular grid with these partial derivative approximations.

Figure 3 presents two plots of truncation error, using the first- through fourth-order terms of Equation (9). The calculations for both plots use the R1 grid velocity and the elevation solutions for derivative estimations. However, node distributions are provided from the R1 grid (solid curve) and a variable grid that was designed by the procedure described below (dotted curve). For a regular grid ($\Delta_i = \Delta_{i+1}$), the odd orders cancel out leaving only a plot of the second- and fourth-orders of the truncation error series (solid curve). The greatest local truncation error is found at the shelf break. Other relatively high error values occur in shallow shelf waters, on the continental slope, at the toe of the continental slope and at the toe of the continental rise.
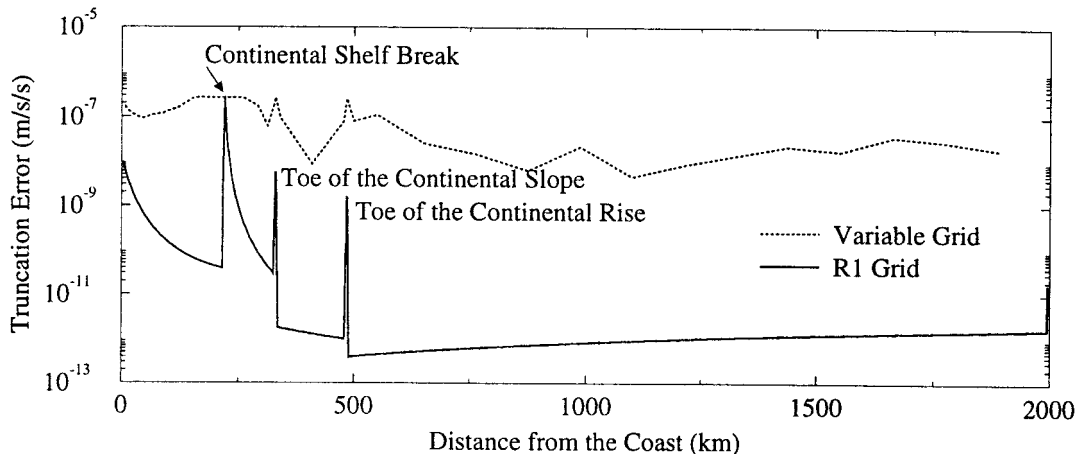

Figure 3. Local truncation error for the 1D momentum equation.

5. LTEA GRIDS BASED ON SOLUTIONS FROM A FINE GRID

If the node distributions were ideal and the solutions were perfect, a plot of the local truncation error would be constant at zero. Although it is impossible to achieve a perfect solution, an optimal number *and* distribution of node points can lead to a more uniform distribution of truncation error (dotted curve, Figure 3).

A dramatic reduction in the cost of the solution (where cost is a function of the total number of nodal points) is realized when node spacing requirements are based on an LTEA. By relaxing the grid size in regions where the truncation error is low, a grid is constructed that displays a more uniform distribution of such. For demonstration purposes, assume that the magnitude of the peak local truncation error, at the continental shelf break, is sufficiently low at $\tau_{max} = 2.81 \times 10^{-7}$ m/s [2]. Equation (9) is set equal to τ_{max} and the local node spacing (Δ_i) is determined, which maintains τ_{max} throughout the domain. Note that the procedure is valid regardless of how one defines the acceptable level of error.

Figure 4 presents a plot of four separate node spacing requirements, which govern the maximum allowable spacing between nodes for the respective grids of Figure 5. The curves of Figure 4 (from top to bottom) are generated as follows: using the second-order truncation terms (solid curve) in Equation (10); with Equation (2), the topographic length scale criterion (long/short dashed curve); using the second- and fourth-order truncation terms (dashed curve) in Equation (10); and with Equation (1), the wavelength to Δx criterion (dotted curve).

Figure 4 shows that LTEA-based spacing requirements are reduced by the inclusion of the fourth-order with the second-order terms. This addition results in a significantly higher level of resolution in the deep ocean and on the continental rise, when compared with the second-order only node spacing requirements. Inclusion of the fourth-order with the second-order terms also results in a node spacing of 12.5 km at the toe of the continental rise compared with the second-order condition of 36 km. In addition, at the toe of the continental slope, the LTEA-based method shows a reduction from 16.8 to 8.5 km with the inclusion of the fourth-order terms.

The reduction in the node spacing requirements is explained by performing an analysis of the variables ($\hat{u}_j$ and $\hat{\eta}_j$) of Equation (10) and their spatial derivatives [14]. The analysis shows that the second-order truncation terms are competing with the fourth-order truncation terms in deeper water. In fact, the fifth spatial derivative of $\hat{\eta}_j$ dominates the third spatial derivative of $\hat{\eta}_j$ in deeper water, i.e. on the continental rise and in the deep ocean. When this occurs, Δ_i is reduced in order to produce a uniform truncation error distribution. Thus, inclusion of the fourth-order terms drives down the acceptable level of Δ_i in deeper water. This example illustrates that the leading order term does not necessarily dominate the overall behavior of the truncation error.

Figure 4 also provides the node spacing requirements generated using Equation (2), the topographic length scale criterion (long/short dashed curve), and Equation (1), the wavelength to Δx, criterion (dotted curve). In order to achieve a resolution similar to that produced with the second- and fourth-order LTEA, α of Equation (2) is set equal to 0.315. In addition, a deep ocean spacing of approximately 240 km is used for this employment of the topographic length scale criterion because this distance is near the upper limit achieved at the toe of the continental rise. Equation (1), the wavelength to grid size ratio criterion, is set equal to a
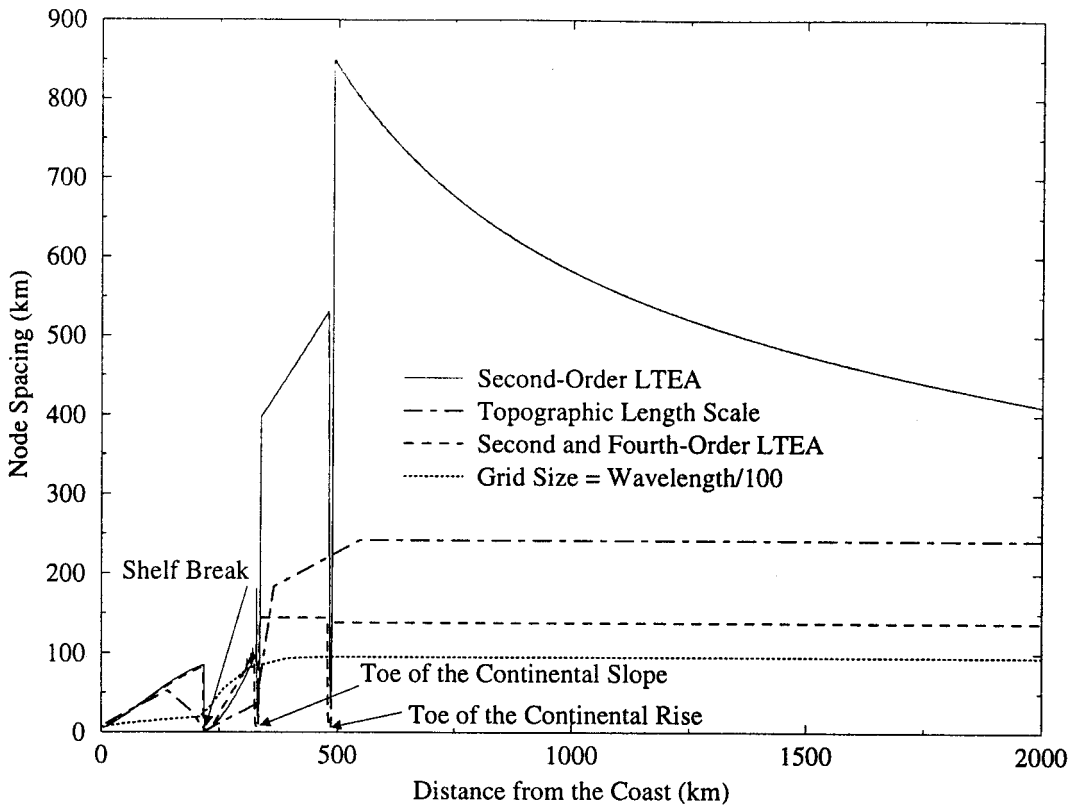
Figure 4. Node spacing requirements based on: a second-order LTEA of the momentum equation; the topographic length scale criterion; a second- and fourth-order LTEA of the momentum equation; and the wavelength to Δx ratio criterion.

constant value of 100, which is conservative when compared with values reported in the literature (≤ 40) [10,15], and the grid size is computed (dotted curve in Figure 4) for the 1D domain presented in Figure 2.

The local node spacing requirements (Figure 4) are used as a maximum allowable limit for finite element grid generation. The mesh generation procedure is also constrained by the domain length in that the sum of the local node spacings must equal the domain length.

A grid is also produced by basing it on a first- through fourth-order LTEA. This procedure, which incorporates the first four terms of Equation (9), is complicated by the fact that adjacent element sizes, Δ_i and Δ_{i+1}, must be known. Therefore, computation of node spacings begins at the continental shelf break where τ_{max}, the peak truncation error, is found and where the spacing (1 km) required to attain this level of truncation error is known. Application of this procedure allows an element-by-element progression towards the shoreline, by using the node spacing to the right when computing a new one to the left. The converse procedure is followed from the continental shelf break towards the open ocean boundary [14].
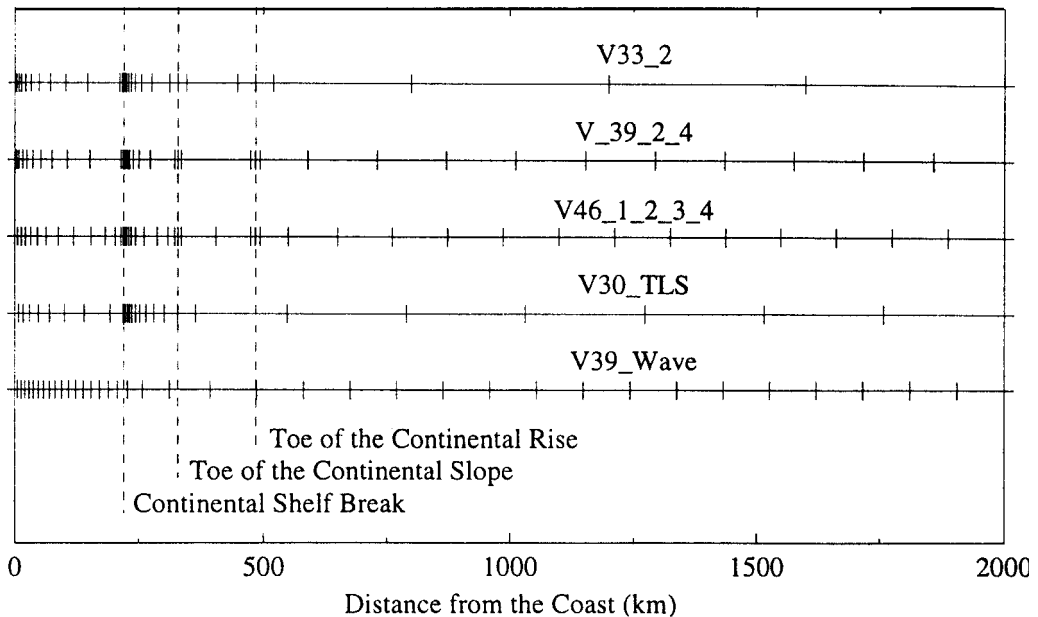
Figure 5. A comparison of five variable 1D grids, which are based on: LTEA (V33_2, V39_2_4 and V46_1_2_3_4); the topographic length scale criterion (V_30_TLS); and the wavelength to Δx ratio criterion (V39_Wave).

Table III and Figure 5 summarize the resulting grids based on the local node spacing requirements (Figure 4) and the grid based on a first- through fourth-order LTEA. Table III designates a name for each of the finite element grids (column 1), which indicates the number of nodes and the procedure used to produce the mesh. Note that all grids have approximately the same number of nodes. Figure 5 presents a graphical representation of each of the five meshes. Vertical dashed lines delineate discontinuities in the topographical bathymetric gradient. Note that all but one of the five grids, grid V39_Wave, differ significantly from practical grids reported in the literature, *viz* all except grid V39_Wave define the minimum spacing at the continental shelf break and not at the shoreline.

Table III. Grids based on alternative node spacing requirements

Grid	Based on	Imposed maximum multiple of change
V33_2	Second LTEA	No imposed limit
V39_2_4	Second and fourth LTEA	No imposed limit
V46_1_2_3_4	First through fourth LTEA	No imposed limit
V30_TLS	Topographic length scale	No imposed limit
V39_Wave	Wave/$\Delta x = 100$	No imposed limit

One major difference sets grid V46_1_2_3_4 apart from all of the others. The extra nodes of this grid are associated with a gentler relaxation of node spacing when one topographic gradient transitions to the next (Figure 5). However, the more gradual variation in element sizes with grid V46_1_2_3_4 is predominantly a result of node placement and not node addition. This grid has the lowest rate of change in element size.

Grid V30_TLS increases resolution on the deep ocean-side of the shelf break (Figure 5) because the slope has the highest gradient of depth, which is captured by the first-order derivative of Equation (2). However, node spacing requirements based on LTEA utilize derivatives of the response variables and thereby promote increased resolution where there are high gradients in the solution, which is not necessarily limited to steep topographical gradients.

It should also be noted from Figure (5) that the wavelength to grid size ratio grid, V39_Wave, displays the highest resolution in the deep ocean and has the most uniform spacing of any of the five grids.

Each of the five variable grids is used in a simulation of 10 days of real time with a 4 s time step following the procedure outlined in the Section 2. Error calculations are performed for each individual simulation by computing Equations (5a) and (5b) at every node of the R.25 grid. The average of the errors is plotted against the number of nodes in the log–log plots of Figures 6 and 7. Each figure contains four error plots: (a) percent velocity amplitude; (b) absolute velocity phase; (c) percent elevation amplitude; and (d) absolute elevation phase. Average errors over the entire domain and over the continental shelf region, from the coastal boundary to the shelf break, are shown in Figures 6 and 7 respectively.

Because it is known that the Galerkin, linear, finite element solution exhibits between first- and second-order-accuracy (degraded accuracy appears to be related to boundary condition implementation [8]), each individual plot in Figures 6 and 7 includes a first-order (dashed line) and a second-order curve (solid line), which intersects the particular error associated with grid V46_1_2_3_4 (upright triangle symbol). If the total number of elements for this grid was doubled or halved, with a size proportional to the existing elements, the resulting error would fall somewhere between the range of the first- and the second-order curves. This permits the evaluation of the performance of these finite element meshes on a per node basis. One can draw a vertical line through any of the error plots and compare it with grid V46_1_2_3_4. For example, if a point lies above the first- and second-order lines, the associated grid has not performed as well as grid V46_1_2_3_4. These curves indicate that, in general, the LTEA-based grid V46_1_2_3_4 outperforms all other grids on a per node basis.

Consider the graphical representations of the grids in Figure 5, in particular the uniform level of high resolution provided over the continental shelf by grid V39_Wave. On the basis of this resolution, one may expect this grid to perform well over the continental shelf region, especially if the source of error is assumed to be *local*. However, Figure 7 clearly shows that the wavelength to Δ_x ratio criterion (asterisk symbol) produces a grid that performs poorly over the shelf region, relative to grid V46_1_2_3_4.

Of the eight error plots shown in Figures 6 and 7, there is only one occurrence where another grid clearly outperforms grid V46_1_2_3_4 (Figure 6(b)). This is a direct result of the extremely low, *average* absolute velocity phase error associated with grid V39_Wave in the deep ocean region and the fact that the deep ocean region constitutes over 75% of the entire domain. Of significance is the fact that grid V46_1_2_3_4 outperforms grid V39_Wave over
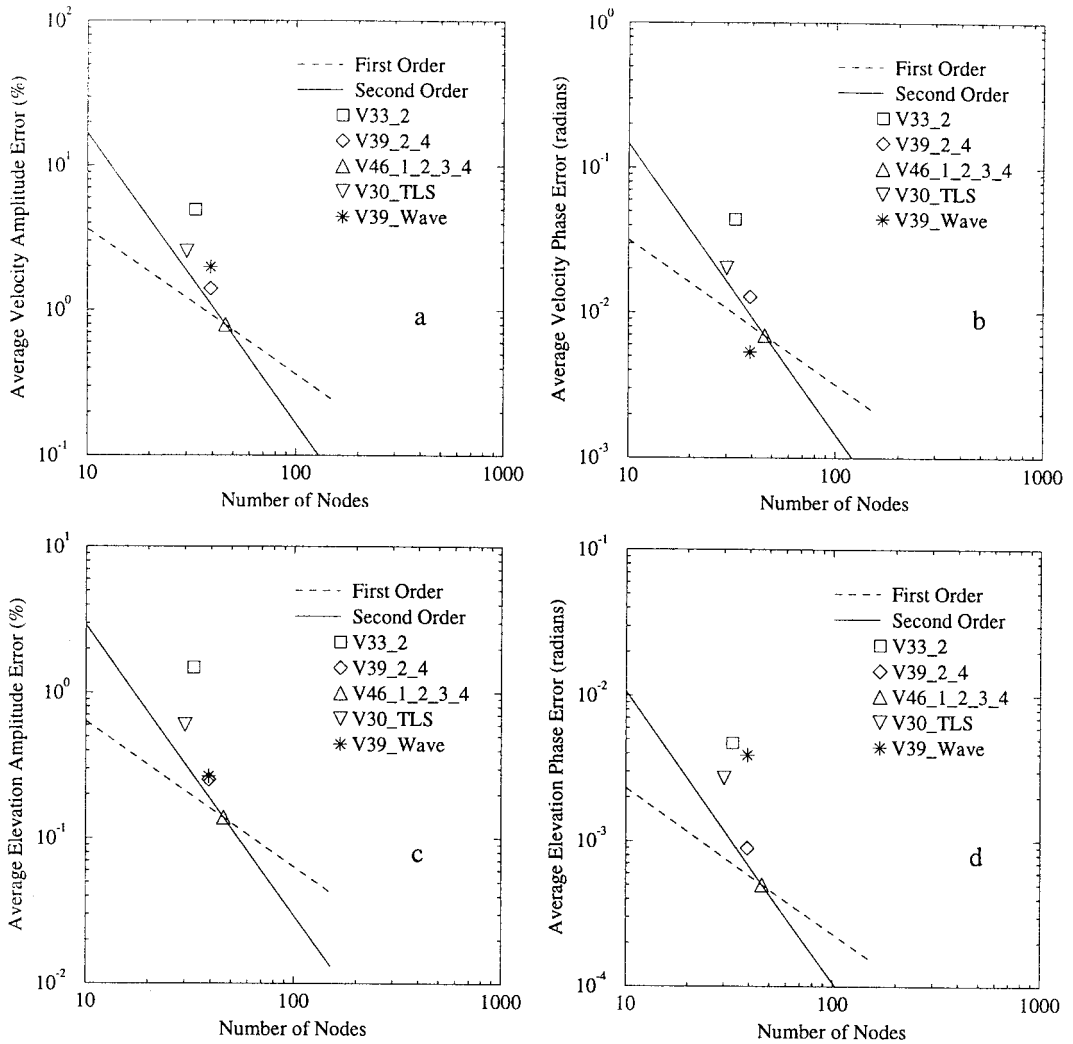
Figure 6. Average errors over the entire domain, associated with the grids of Table III and Figure 5: (a) percent velocity amplitude; (b) absolute velocity phase; (c) percent elevation amplitude; and (d) absolute elevation phase.

the deep ocean region with respect to absolute elevation phase. When one takes into account the fact that grid V46_1_2_3_4 has a deep ocean node spacing of 112.5 km, versus 95 km for grid V39_Wave (> 18% increase in resolution), this becomes an even more dramatic result. The significance lies in the fact that increased resolution located *outside* the deep ocean, illustrated in Figure 5, allows grid V46_1_2_3_4 to outperform grid V39_Wave over the deep ocean region and that resolution is identified by the LTEA-based method.
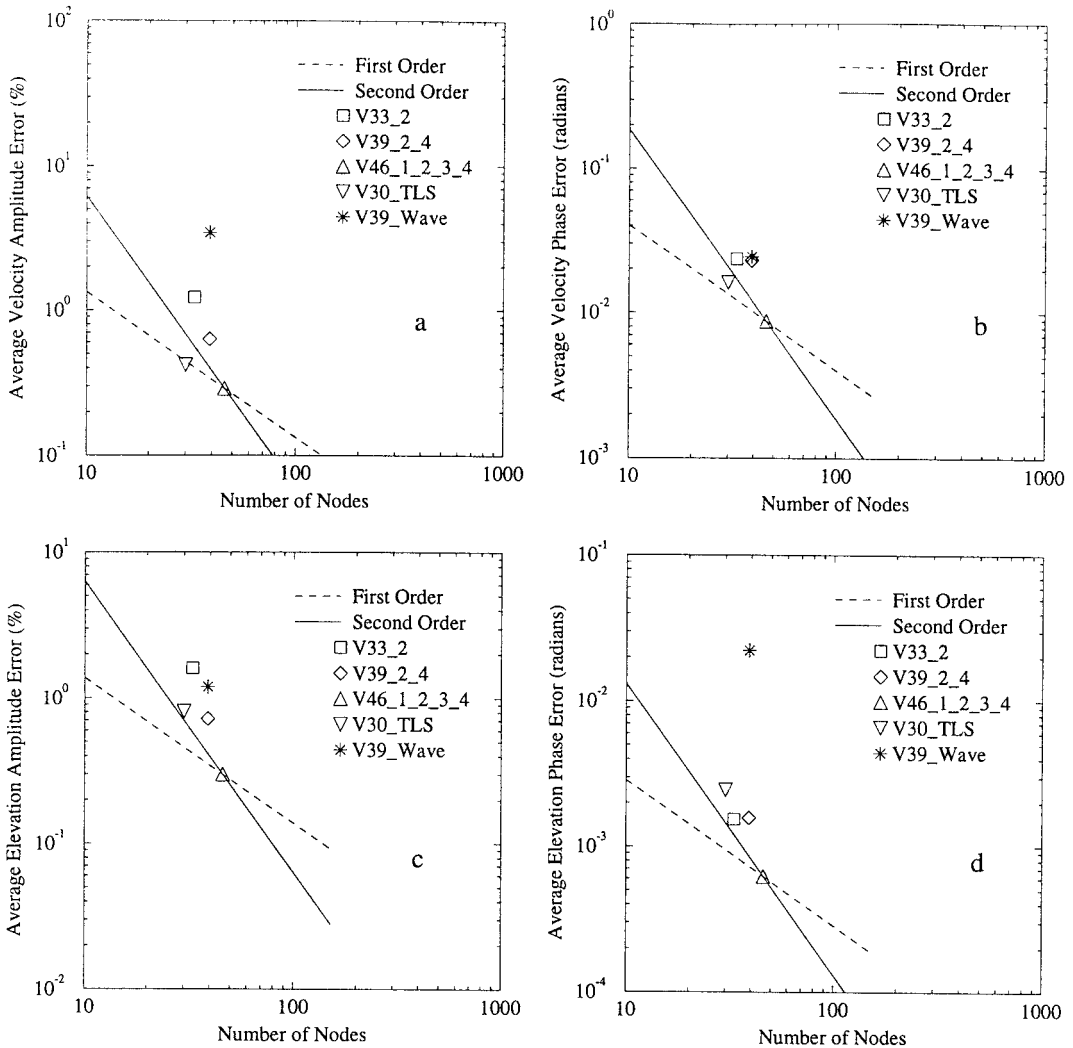
Figure 7. Average errors over the continental shelf region, associated with the grids of Table III and Figure 5: (a) percent velocity amplitude; (b) absolute velocity phase; (c) percent elevation amplitude; and (d) absolute elevation phase.

Close examination of the plots included in Figures 6 and 7 also indicates that grid V30_TLS (inverted triangle symbol), which is based on the topographic length scale criterion, performs well, especially over the continental shelf region. In addition, it is noted from Figure 6 that grid V39_2_4 (diamond symbol) performs consistently well, particularly relative to grid V33_2 (square symbol).
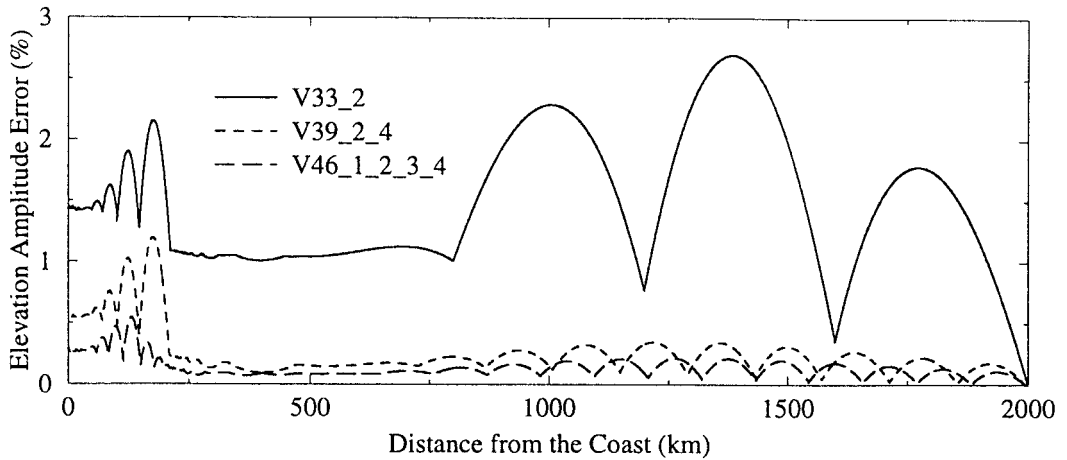
Figure 8. Percent elevation amplitude errors associated with the LTEA-based grids of Table III and Figure 5, when normalized by the comparison solution (R.25).

Figure 8 displays a plot of the percent elevation amplitude errors for the LTEA-based grids versus spatial location. Equation (5a) is used to compute elevation amplitude errors at each node of grid R.25. The peak error is drastically reduced by inclusion of higher order terms when generating LTEA-based grids. Note that inclusion of the fourth-order terms in the LTEA results in an increase of nodes from 33 to 39, with the six extra nodes appearing in the deep ocean region. The six extra nodes of grid V39_2_4 significantly reduce all measures of error, not only in the deep ocean but also throughout the domain (short-dashed curve, Figure 8). Furthermore, Figure 8 highlights the importance of incorporating the first through fourth even- *and* odd-order terms in the LTEA (long-dashed curve, grid V46_1_2_3_4), which effectively reduce elemental expansion rates (Figure 5). It is also noted that the errors associated with grid V46_1_2_3_4 decrease on the continental shelf when compared with grid V39_2_4.

6. AN IMPOSED MAXIMUM MULTIPLE OF CHANGE CRITERION

A strict interpretation of the LTEA-based node spacing requirements results in the generation of accurate, efficient 1D grids. However, the ultimate goal is to develop a workable algorithm based on LTEA for generating 2D finite element grids. This involves taking advantage of what has been learned thus far from the detailed LTEA in order to enact a numerically sound, yet simplified, criterion. Ideally, this criterion would limit the LTEA to the second- and fourth-order truncation error terms, thereby eliminating the need to know adjacent element sizes (a considerable simplification because it eliminates the domain-wide interdependence of the grid, which is related to the odd-ordered terms). Note that even if the mesh is generated by

considering only the even-order terms, the contribution of the odd-order terms to the solution's total truncation error will not be eliminated because the following will continue to be true: $|\Delta_i - \Delta_{i+1}| \geq 0$.

The prerequisite demands may be met by a grid generation algorithm incorporating an imposed maximum multiple of change. In developing equations for truncation error, it was noted that as Δ_i approaches Δ_{i+1}, the odd-order truncation terms become less significant and ultimately cancel out when Δ_i equals Δ_{i+1}. As a result, the magnitude and relative importance of the remaining even-order terms change. Furthermore, note that there are certain stretches on the plot of LTEA-based node space requirements (Figure 4) where a maximum multiple of change of 1.4 is imposed. The knowledge of the multiple of change is used in this section to interpret the node spacing requirements.

Table IV summarizes the grids produced by imposing a maximum multiple of change when interpreting the LTEA-based node spacing requirements of Figure 4. Three distinct meshes are generated for each of two different LTEAs: the second-order LTEA; and the second- and fourth-order LTEA. The maximum multiple of change is given the values of 1.4, 1.2 and 1.1 for each set. If the local node spacing requirements warrant a lower multiple of change than what is imposed, the lower value is used.

Simulations of 10 days of real time are performed for each grid, as outlined in Section 2, with a 4 s time step. Figure 9 contains four error plots for the entire domain: (a) percent velocity amplitude; (b) absolute velocity phase; (c) percent elevation amplitude; and (d) absolute elevation phase. Each error plot of Figure 9 contains log–log plots of errors associated with the three LTEA-based grids of the previous section (denoted with plus, $\times$ and asterisk symbols) and six LTEA-based grids, each with a maximum multiple of change (triangular symbols). When the multiple of change is equal to 1.4, the triangular symbols point to the left; for a multiple of change equal to 1.2, the triangular symbols point downward; and for the multiple of change equal to 1.1, the triangular symbols point to the right. Clear triangular symbols denote grids that are based on a second-order LTEA, while filled triangular symbols signify those based on a second- and fourth-order LTEA. Each plot also contains three second-order-accurate curves, one passing through each of the error points associated with the three LTEA-based, strictly interpreted grids: V33_2; V39_2_4; and V46_1_2_3_4. In addition, three LTEA-based grids, which utilize coarse grid solutions (circle, square and diamond symbols) are included and will be discussed in the next section.

Table IV. Grids generated using R1 with an imposed maximum multiple of change

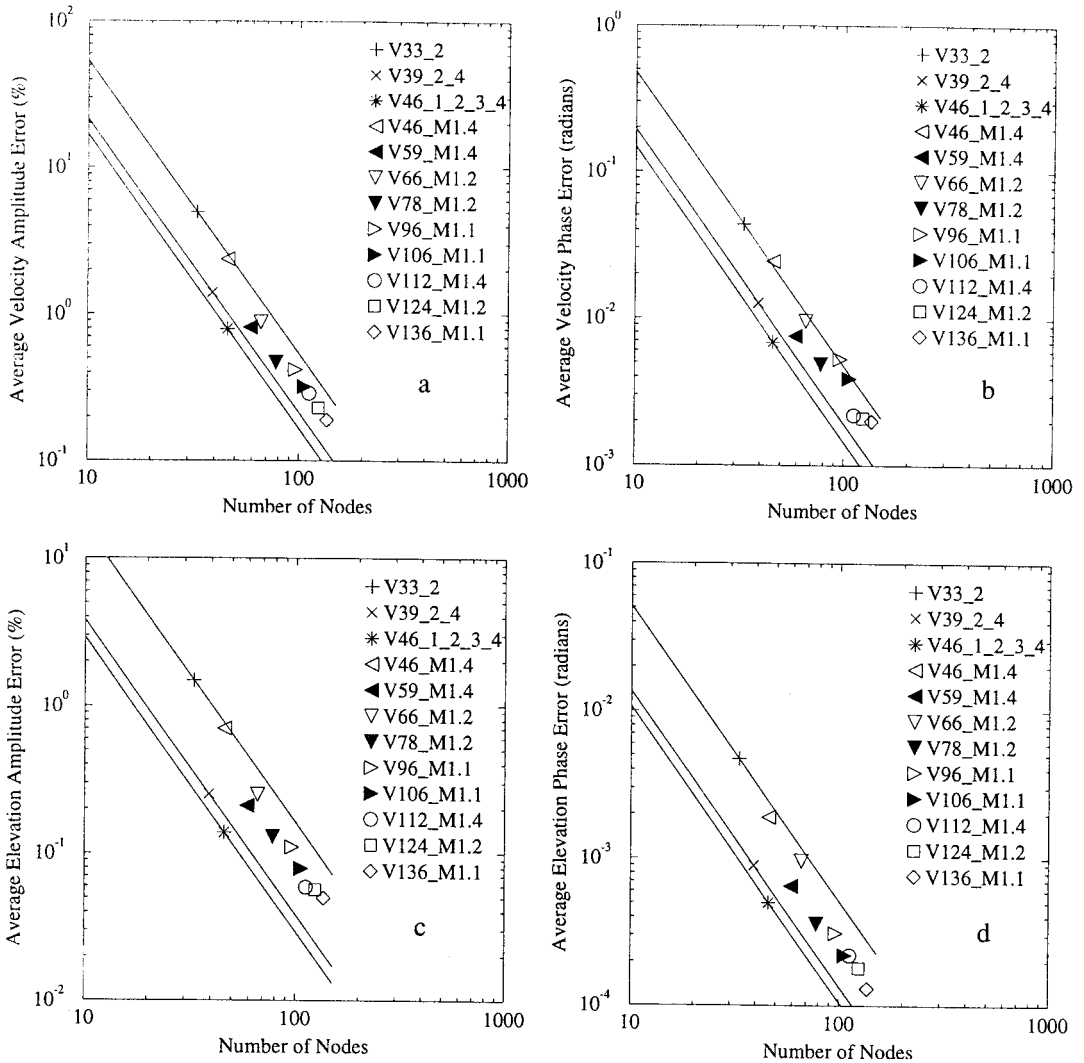| Grid	Based on truncation errors	Imposed maximum multiple of change
V46M 1.4	Second	1.4
V59M 1.4	Second and fourth	1.4
V66M 1.2	Second	1.2
V78M 1.2	Second and fourth	1.2
V96M 1.1	Second	1.1
V106M 1.1	Second and fourth	1.1

Figure 9. Average errors over the entire domain, associated with LTEA-based grids: (a) percent velocity amplitude; (b) absolute velocity phase; (c) percent elevation amplitude; and (d) absolute elevation phase.

Note the similarity of the curve sets (second-order-accurate curves that are plotted through the plus, × and asterisk symbols in Figure 9) associated with the three LTEA-based grids of the previous section. Each set of curves has a large gap between the V33_2 and the V39_2_4 curves, and a relatively close proximity between the V39_2_4 and the V46_1_2_3_4 curves, with the latter being more accurate on a per node basis. This indicates that the solutions are converging, as more terms are included in the respective LTEA. In all of the plots of Figure

9, the error reduction appears to be exhibiting second-order behavior. All but one (Figure 9(b), V46M_1.4) of the errors associated with the maximum multiple of change grids fall between the V33_2 and the V39_2_4 curves. With regard to the second-order LTEA-based grids (Figure 9, clear triangles), this is noteworthy; it indicates that imposing a maximum multiple of change with the second-order LTEA-based grids results in an error level below that of a strictly interpreted second-order mesh. None of the error points associated with the multiple of change grids that are based on a second- and fourth-order LTEA fall to the left of the second-order curve associated with grid V39_2_4. The multiple of change grids are less efficient because the conservative multiple of change criterion requires some nodes where they may not be needed.

7. LTEA GRIDS BASED ON SOLUTIONS FROM A COARSE GRID

Successful implementation of the maximum multiple of change criterion indicates a potential for generating 2D LTEA-based finite element grids. However, one major requirement holds back that development; all of the LTEAs have utilized solutions from the highly resolved R1 grid for estimating derivatives. While the use of a grid with 1 km spacing in 1D does not pose a problem, a fine grid with 1 km spacing when applied to a large 2D domain, such as the WNAT model domain of Figure 1, would prove to be too computationally expensive.

As an example of an alternative approach, a coarse 101 node grid is defined with a regular spacing of 20 km (R20 grid). The numerically computed solutions from grid R20 are used to approximate the derivative terms in Equation (10). Use of the R20 grid stretches out the nodes at which the derivatives are estimated for the LTEA, which tends to smooth the truncation errors over larger regions, as is shown in Figure 10. Note how the coarser grid (solid line)
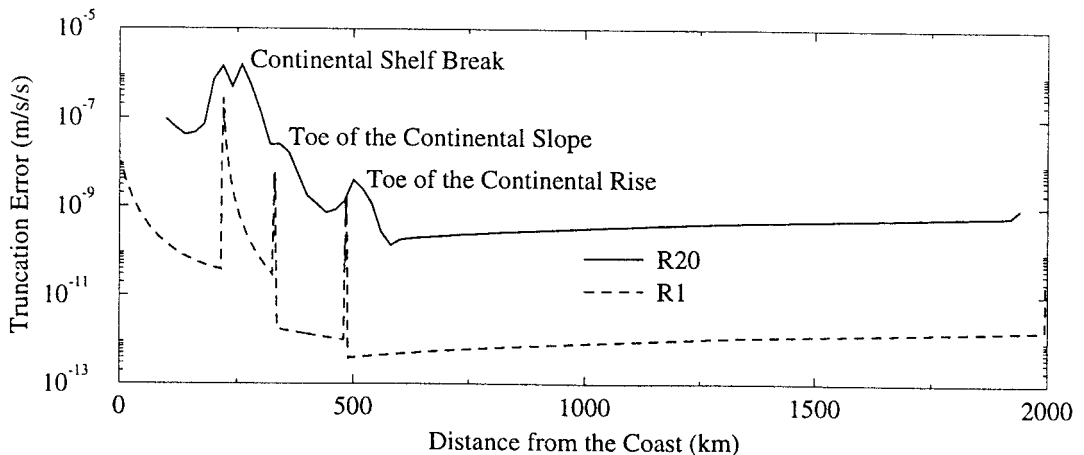

Figure 10. Local truncation error for the 1D momentum equation using the R20 and the R1 grid.

Table V. Grids generated using R20 with an imposed maximum multiple of change

Grid	Based on truncation errors	Imposed maximum multiple of change
V112M 1.4	Second and fourth	1.4
V124M 1.2	Second and fourth	1.2
V136M 1.1	Second and fourth	1.1

distributes the peaks relative to the fine grid (dashed line); in addition, note that the magnitude is larger for the R20 grid, but the spatial error distribution is preserved.

Equation (10) is set equal to the peak truncation error, which in this case is that associated with the R20 grid solutions, and, subsequently, the minimum local node spacing requirement will be 20 km, i.e. the resolution of the R20 grid. In order to compare LTEA-based R20 grids with LTEA-based R1 grids, all local R20 grid LTEA-based node spacing values are multiplied by 1/20 (smallest spacing required/regular spacing) such that the minimum local spacing is l km.

Table V shows the grids used for this study of LTEA-based grids from coarse solutions. Three separate grids are generated, using an imposed maximum multiple of change of 1.4, 1.2 and 1.1. All grids are based on a second- and fourth-order LTEA using the R20 grid to estimate the derivatives.

As is mentioned in the previous section, the errors associated with 10-day simulations of real time with 4 s time steps and each of these practical method grids are plotted in Figure 9 (denoted by the circle, square and diamond symbols). On an error per node basis, these grids correspond nicely with the maximum multiple of change grids of the previous section. The error continues to decline with second-order behavior, as is seen in the previous section. The implementation of a more economical approach (this time not only by imposing a maximum multiple of change but also by using a coarser grid to estimate derivatives in the truncation series expansions) results in a method that is more accurate overall, but is less computationally efficient than the strict interpretation.

8. CONCLUSIONS

This study into 1D finite element grid generation demonstrates that LTEA provides a basis for grid generation by more thoroughly coupling the physics, as represented by discrete equations, underlying tidal flow and circulation to the node placement process. The competition between orders of the truncation error series, which indicates that the leading order term is not always dominant, provides a noteworthy corollary.

The LTEA-based method, as well as the topographic length scale criterion, requires the highest resolution at the continental shelf break and not at the shoreline, which is contrary to common practice. It is noted that the grid based on the topographic length scale performed well in the shelf regions and is suggested that a combination of the topographic length scale criterion and the wavelength to grid size ratio criterion could provide reasonable grid resolution. However, the LTEA-based method produces the most accurate grids when

evaluated on a per node basis. As was noted when comparing Figures 5 and 8, finite element grids based on an LTEA goes to the *source* of error, which improves both local *and* global results.

The imposed maximum multiple of change is justified as a sound, numerically-based criterion because it limits the contribution of both even- and odd-order terms of the truncation series expansions. Finally, a second variation on the LTEA-based method is introduced that utilizes solutions from a coarse grid (20 km) to estimate derivatives for the LTEA. The success of these variations are important, because of the enhanced feasibility of a 2D application that will be more directly coupled to 2D physical features and processes that they are intended to simulate.

REFERENCES

1. D.R. Lynch and W.G. Gray, 'A wave equation model for finite element tidal computations', *Comput. Fluids*, **7**, 207–228 (1979).
2. D.R. Lynch, 'Progress in hydrodynamic modeling, review of U.S. contributions, 1979–1982', *Rev. Geophys. Space Phys.*, **21**, 741–754 (1983).
3. I.P.E. Kinnmark, 'The shallow water wave equations: formulation, analysis and application', *Ph.D. Dissertation*, Department of Civil Engineering, Princeton University, NJ, 1984.
4. J.J. Westerink and W.G. Gray, 'Progress in surface water modeling', *Rev. Geophys.*, **29**, 210–217 (1991).
5. R.A. Luettich Jr., J.J. Westerink and N.W. Scheffner, 'ADCIRC: an advanced three-dimensional circulation model for shelves, coasts and estuaries, Report 1: theory and methodology of ADCIRC-2DDI and ADCIRC-3DL', *Technical Report DRP-92-6*, Department of the Army, 1992.
6. M.G.G. Foreman, 'An accuracy analysis of boundary conditions for the forced shallow water equations', *J. Comput. Phys.*, **64**, 334–367 (1986).
7. J.J. Westerink, R.A. Luettich Jr., J.K. Wu and R.L. Kolar, 'The influence of normal flow boundary conditions on spurious modes in finite element solutions to the shallow water equations', *Int. J. Numer. Meth. Fluids*, **18**, 1021–1060 (1994).
8. R.L. Kolar, W.G. Gray and J.J. Westerink, 'Boundary conditions in shallow water models-an alternative implementation for finite element codes', *Int. J. Numer. Meth. Fluids*, **22**, 603–618 (1996).
9. C.A. Blain, J.J. Westerink and R.A. Luettich Jr., 'The influence of domain size on the response characteristics of a hurricane storm surge model', *J. Geophys. Res.*, **99**, **C9**, 18467–18479 (1994).
10. J.J. Westerink, R.A. Luettich Jr. and J.C. Muccino, 'Modeling tides in the western North Atlantic using unstructured graded grids', *Tellus*, **46A**, 178–199 (1994).
11. J.J. Westerink, J.C. Muccino and R.A. Luettich Jr., 'Resolution requirements for a tidal model of the Western North Atlantic and Gulf of Mexico', in T.F. Russell *et al.* (eds), *Proceedings of the IX International Conference on Computational Methods in Water Resources*, Computational Mechanics Publications, Southampton, 1992.
12. R.A. Luettich Jr. and J.J. Westerink, 'Continental shelf scale convergence studies with a barotropic tidal model', in D.R. Lynch and A.M. Davies (eds), *Quantitative Skill Assessment for Coastal Ocean Models*, A.G.U., **47**, 349–371 (1995).
13. S.C. Hagen and J.J. Westerink, 'Finite element grid resolution based on second and fourth-order truncation error analysis', in C.A. Brebbia, L. Traversoni and L.C. Wrobel (eds.), *Computer Modelling of Seas and Coastal Regions: Proceedings of the 2nd International Conference*, 1995, Computational Mechanics Publications, Southampton, pp. 283–290.
14. S.C. Hagen, 'Finite element grids based on a localized truncation error analysis', *Ph.D. Dissertation*, Department of Civil Engineering and Geological Sciences, University of Notre Dame, IN, 1998.
15. C. Le Provost and P. Vincent, 'Some tests of precision for a finite element model of ocean tides', *J. Comput. Phys.*, **65**, 273–291 (1986).

16. C.G. Hannah and D.G. Wright, 'Depth dependent analytical and numerical solutions for wind-driven flow in the coastal ocean,' in D.R. Lynch and A.M. Davies (eds), *Quantitative Skill Assessment for Coastal Ocean Models*, A.G.U., **47**, 125–152 (1995).
17. M.J. Berger and P. Colella, 'Local adaptive mesh refinement for shock hydrodynamics', *J. Comput. Phys.*, **82**, 64–84 (1986).
18. R. Lohner, 'An adaptive finite element scheme for transient problems in CFD', *Comput. Methods Appl. Mech. Engng.*, **61**, 323–338 (1987).
19. J.T. Oden, L. Demkowicz, W. Rachowicz and T.A. Westermann, '*A posteriori* error analysis in finite elements: the element residual method for symmetrizable problems with applications to compressible Euler and Navier–Stokes equations', *Comput. Methods Appl. Mech. Engng.*, **82**, 183–203 (1990).
20. S. Chang and D.C. Haworth, 'Kinetic-energy-balance based solution-adaptive mesh refinement', in R.W. Johnson and E.D. Hughes (eds), *Quantification of Uncertainty in Computational Fluid Dynamics*, **213**, American Society of Mechanical Engineers, New York, 1995, pp. 7–12.
21. A.S. Franca, K. Haghighi and L.S. Oliveira, 'Error estimation and adaptivity in finite element analysis of transport problems', in R.W. Johnson and E.D. Hughes (eds), *Quantification of Uncertainty in Computational Fluid Dynamics*, **213**, 1995, pp. 19–24.
22. P.J. Roache, 'Perspective: a method for uniform reporting of grid refinement studies', *J. Fluids Eng.*, **116**, 405–413 (1994).